Plasma Chemistry and Plasma Processing, Vol. 14, No. 3, 1994

Particle Densities and Non-Equilibrium in a Low-Pressure Argon Plasma Jet

Steven P. Fusselman[1] and Hirotsugu K. Yasuda[1]

Received December 29, 1992; revised December 17, 1993

Plasma diagnostic techniques have been employed to determine particle densities and temperatures in a low-pressure argon plasma jet generated by a cascade arc. These measurements allow characterization of the extent to which the plasma jet deviates from thermodynamic equilibrium and provide a basis for predicting how reactive gases will interact with the excited and ionized species in the plasma jet. It was found that the distribution of atomic states in the plasma jet is not adequately described by either local thermodynamic equilibrium (LTE) or partial local thermodynamic equilibrium (pLTE), and the jet was optically thick for 3p→4s transitions across the jet radius. Excited argon neutrals outnumber ions by a large ratio, and dominate subsequent dissociation/excitation phenomena. The rate of methane destruction in the plasma jet shows that estimates for particle densities, temperature, and jet velocity are self-consistent.

KEY WORDS: Plasma jet; nonequilibrium plasma; plasma diagnostics; excited argon; cascade arc.

1. INTRODUCTION

Plasma polymerization and plasma surface modification processes have a vast array of potential applications. Typically, commercial exploitation of these processes is limited by economic rather than technical considerations, due to low process throughput. The cascade arc plasma source may allow the attainment of high throughput, as it delivers a high flux of excited and ionized species to the treated surface in a directed beam. Results from D. C. Schram's group at Eindhoven University of Technology in The Netherlands have demonstrated that very high deposition rates over relatively large areas can be achieved with the cascade arc[1-6].

The objective of the present work is to obtain estimates for excited and ionized argon densities, gas temperature, electron temperature, and jet

[1]Center for Surface Science and Plasma Technology, Department of Chemical Engineering, University of Missouri-Columbia, W2033 Engineering Building East, Columbia, Missouri 65211.

0272-4324/94/0900-0251$07.00/0

velocity for an argon plasma jet generated in a cascade arc plasma source. These results will be used to determine whether existing plasma models adequately describe this low-pressure argon jet, and to determine the minimum information required to specify the atomic state distribution function (ASDF), that is, the population distribution among various energy levels for ions and neutrals in a plasma. This information is also used to predict interaction between "monomer" or reactive gas with excited or ionized argon in the plasma jet.

As noted by van der Mullen in a series of review articles,[7-9] more information is required to describe the atomic state distribution function as a plasma departs further from thermodynamic equilibrium. Chang and Pfender[10] concluded that low-pressure argon plasma jets deviate substantially from local thermodynamic equilibrium (LTE), although LTE apparently is adequate for describing plasma jets operated at atmospheric pressures. For the low-pressure argon plasma jet obtained from a cascade arc, predicting the ASDF is further complicated by large and sudden changes of pressure and temperature between the cascade arc column and the vacuum chamber. This sudden change in conditions affects not only the various coefficients for rate and transport processes, but also the rate at which two-body (such as ionizing collisions between excited argon neutrals) and three-body (such as three-body association to form molecular argon ions or three-body recombination) collisions occur. In light of the abrupt departure from conditions in the cascade arc column, it was anticipated that differences in the rates at which relaxation processes occur for the various species will lead to populations of these species which are not amenable to description by conventional models.

In the present work, visible light emitted from the plasma jet is analyzed to estimate jet temperature and the densities for excited argon neutrals, and a double Langmuir probe is used to estimate electron density and temperature at several axial positions in the plasma jet. Residual gas analysis is used to estimate the extent of methane consumption in the plasma jet. The applicability of various plasma models for description of the argon ASDF in the plasma jet is also evaluated.

2. EQUIPMENT AND EXPERIMENTAL METHODS

2.1. Equipment

The major components of the cascade arc reactor are the cascade arc plasma source, the vacuum chamber (reactor vessel), the process equipment, and the diagnostic equipment.

The cascade arc was fabricated by Progressive Prototype, of Columbia, Missouri. A single 1/16″ (1.6 mm) diameter tungsten tip serves as the

cathode. The tip is located on the column axis and is held in place by a crimp/collet assembly which allows uniform argon flow over the tip. A ceramic (Macor) insert is placed between the collet and the first disk in the column to prevent arc transfer between the tip and first disk. The copper disks which form the cascade arc column are machined from a 99% Cu/1% Te alloy, which was also used for the cathode holder and crimp/collet device. A 5/32″ (3.9 mm) diameter column is formed through which the arc discharge is established. The 7/16″ (11.1 mm) thick, 2″ (50.8 mm) diameter copper disks are insulated from each other by 1 mm thick silicone rubber spacers. An ethylene glycol–water mixture is circulated through each disk by way of 1/4″ (6.4 mm) o.d. copper tubes inserted through the outer walls of the disks. Usually, nine disks are employed in the column for a total length of 10.5 cm. Two 1/4″ NPT threaded holes centered $2\frac{1}{4}$″ (52.7 mm) off the jet axis and directly opposite each other serve as the monomer feedthrough and pressure measurement tap. At the monomer feedthrough, a second 1/4″ NPT threaded hole on the vacuum side allows the dispersal ring to be fastened to the support plate. The dispersal ring has four 1/32″ (0.8 mm) diameter holes placed symmetrically about the center to allow a more even distribution of monomer and/or reactive gases about the plasma jet. Optical components (described later) can also be installed at the support plate.

The vacuum chamber (Fig. 1) consists of the following Pyrex glassware: a 6″ (152.4 mm) i.d. glass cross, 6″–4″ i.d. reducer, and a 4″ (101.6 mm) i.d. *y*-section. The glass cross is 18″ (457 mm) from port to port, the reducer is 9″ (229 mm), and the *y*-section is 14″ (356 mm) along the straight run. The cascade arc is mounted to the cross port opposite the reducer, and the branch on the *y*-section serves as the gas exhaust port.

A 2″ (50.8 mm) i.d. stainless steel tee is located between the vacuum chamber and the stainless steel cold trap, with the residual gas analyzer (RGA) sampling valve connected to the $2\frac{3}{4}$″ CF flange on the tee branch. Vacuum is produced by an Edwards High Vacuum EH500A/E2M80 combination pump.

Gas flow rates are controlled with MKS 2259B and 1259C mass flow controllers in conjunction with an MKS 247B readout controller. Pressure readings are obtained with an MKS 220B Baratron capacitance manometer, and vacuum chamber pressure is controlled with an MKS 253A throttle valve/MKS 252A valve controller, with the throttle valve located between the cold trap and vacuum pump. Arc current is drawn from an Advanced Energy MDX-5K dc power supply.

Ultrahigh purity argon (99.999%) from Linde was used as the carrier gas in the cascade arc. CP-grade methane (99.999%) from Matheson was used as the "monomer." These gases were used as received.

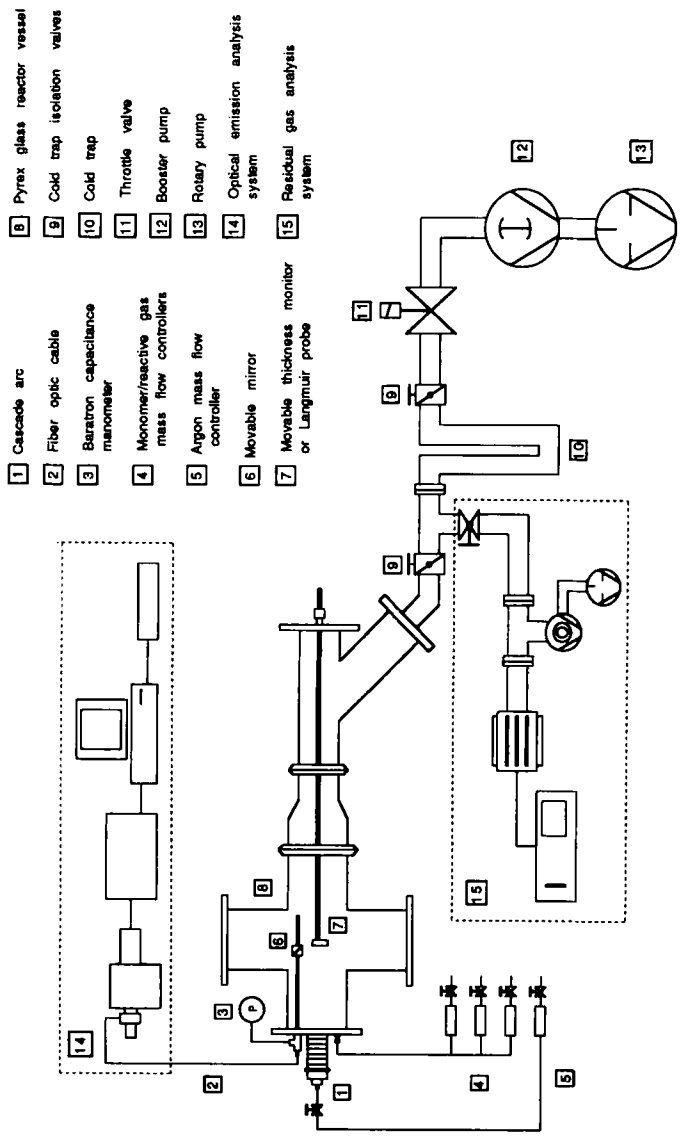

Fig. 1. General schematic of the cascade arc reactor.

The apparatus has three major pieces of diagnostic equipment for analyzing the properties and performance of this process: an optical emission spectroscopic system, a Langmuir double probe system, and a residual gas analyzer.

Light is directed from the plasma jet to the optical emission spectrometer by a 45° mirror and fiber optic cable. The 45° mirror can be centered over any point along the jet axis 2.7 cm to 32.7 cm from the jet inlet, and directs light from the plasma jet to the fiber optic cable, which views the 45° mirror through a Cajon Ultratorr tee mounted on the cascade arc support plate, and observes a 2.5° cone bounded by the 1/4″ NPT fitting in the support plate. The 45° mirror apparatus was manufactured by the University of Missouri Science Instrument Shop. The mirror is an MU-series 1″ × 1″ (25.4 mm × 25.4 mm) square flat mirror manufactured by Optics for Research, and a quartz slide is inserted in a slot in front of the mirror to protect it from any interactions with the plasma jet. A second movable mirror, the reversing mirror, is placed directly opposite the 45° mirror and is used in absorption studies. This MI-series mirror from Optics for Research is a 2″ × 2″ (50.8 mm × 50.8 mm) square by 1/2″ (12.7 mm)) thick flat mirror with surface roughness less than $\lambda/4$. Reflectivity ranges from 92% to 95% over the spectral range of interest. This device was fabricated by the Science Instrument Shop. The reversing mirror is inserted in a bracket which rests on a slotted aluminum support bar, and the position is varied in the same way as the 45° mirror. The aluminum support bar was blackened to eliminate light reflectance when the mirrors are not opposite each other.

Princeton Instruments, Inc. supplied the instrumentation and spectral analysis software. The observable spectral range was 200–1050 nm. A 2-m fiber optic cable is coupled to a variable width (10–2000 μm) slit which is mounted on a Jarrell-Ash Monospec 27 monochromator/spectrograph (crossed Czerny-Turner, 275 mm focal length, $f/3.8$) with a triple grating holder. The three gratings are 150, 600, and 1200 grooves/mm. A Princeton Instruments RY-1024 unintensified diode array detector is mounted at the Monospec 27 exit port, and is controlled by a Princeton Instruments ST120 OSMA detector controller which interfaces with a Dell System 20 computer.

The Langmuir double probe system was manufactured by the M4X Research Group in the University of Missouri-Columbia Nuclear Engineering Department. The probe is mounted in a flange on the straight run port of the 4″ (101.6 mm) y-section. Measurements were taken over the first 25 cm of the plasma jet, and an adjustable support was used to compensate for probe sag at extended axial positions. The probe tips are 1/4″ (6.4 mm) diameter tantalum disks, 0.5 mm thick, and are separated by 5 mm. The probe circuitry and data acquisition setup are proprietary information. Further details may be obtained by contacting Prof. Mark Prelas of the M4X Research Group.

The residual gas analyzer (RGA) is a Leybold-Inficon QX-2000 model with a range of 200 amu. The Faraday cup sensor employed by this unit is attached to a Leybold-Inficon IPC-2 pressure converter system. The major components are the sampling valve, turbomolecular pump (150 liters), and rotary vane pump.

2.2. Experimental Procedures

Before every experiment, the chamber was evacuated to less than 1 mTorr (0.133 Pa) and until the combined outgassing/leak rate was less than the impurity flux from carrier gas.

Optical emission spectra were obtained using a slit width of 15 μm and a photodiode array temperature of -30°C. Background spectra were obtained prior to an experimental run and subtracted from the emission spectra prior to data storage. The 45° and reversing mirror positions were determined by measuring the distance between the positioned rod feedthroughs and a fixed point on the positioning rods. Typical integration times ranged from 5 to 90 s, depending on peak intensities within the 150-nm-wide window being scanned. When absorption data were acquired, the reversing mirror was positioned so that its center was directly opposite the center of the 45° mirror to obtain the reflected intensities, and was placed so that none of its surface was visible to the 45° mirror for nonreflected spectra. The reflected and nonreflected spectra were recorded consecutively without disturbing the spectrograph, so the correspondence between wavelength and diode number was the same for both spectra. Calibration was performed using excited argon neutral lines to relate wavelength to diode number by a polynomial fit. Accuracy of fit was verified by checking other known lines.

The Langmuir double probe position was determined from an indicator attached to the probe driver. The probe position was set, then checked to assure the probe tips were sampling at the jet centerline. Data were obtained at axial positions from 0 to 240 mm every 10 mm for each set of experimental conditions, with the plasma jet operating continuously.

Quantitative RGA data were obtained by recording a mass spectrum for gases present in the isolated IPC-2 to correct for background gases, then recording a spectrum for the carrier gas without monomer and with no plasma to account for impurities, then for the carrier gas with monomer and no plasma, and lastly under plasma conditions with carrier gas and monomer.

3. INTERPRETATION OF DIAGNOSTIC DATA

3.1. Temperature Estimates from the CH($A^2\Delta \rightarrow X^2\Pi$) Band

A gas temperature for the plasma jet is estimated from molecular spectroscopy. The $R(0, 0)$ branch of the CH($A^2\Delta \rightarrow X^2\Pi$) transition was analyzed using the two-temperature model employed by Suzuki and Kuchitsu.[11] In this model, a Boltzmann distribution is assumed locally valid over a few rotational levels. The temperature calculated from lower energy rotational levels, $T_{r,LL}$, corresponds to the gas (i.e., translational) temperature. The temperature calculated from higher rotational levels, $T_{r,UL}$, is more likely dominated by excitation/dissociation processes.

The Boltzmann distribution of rotational levels is described by the equation

$$\frac{d \log_n[I/\nu^3 S]}{d[N'(N'+1)]} = -hcB_{v'}/kT_r \tag{1}$$

where I is the intensity of the emission line corresponding to the transition $N' \rightarrow N''$, ν is the frequency of the transition, S is the line strength for the transition, N' is the rotational level of the emitting state, $B_{v'}$ is the rotational energy level separation for the particular vibrational energy level v' ($14.557\ \text{cm}^{-1}$ for this transition[12]), T_r is the rotational temperature, h is Planck's constant, c is the speed of light, and k is Boltzmann's constant.

The $N' = 7$–9 levels were used to estimate gas temperature, as contributions form $Q(0, 0)$ transitions become quite small and the nearby $R(1, 1)$ transitions are on the shoulders of the $R(0, 0)$ peaks.

3.2. Argon 4*s* and 4*p* Densities from Absorption

Argon 4*s* and 4*p* densities were estimated by measuring the extent to which various lines emitting to these levels were absorbed when reflected back through the plasma jet. The absorption coefficient for a ground-state species as derived by Mitchell and Zemansky[13] is

$$k_0 = \frac{\lambda^2 g_0^2 \sqrt{\ln 2}}{4\pi^{3/2} \Delta\nu_D g_k} N_0 A_t \delta \tag{2}$$

where k_0 is the absorption coefficient, λ is the wavelength of the absorbed light, g_0 and g_k are the statistical weights of the absorbing and emitted states, respectively, $\Delta\nu_D$ is the Doppler half-width of the absorption line, N_0 is the density of the absorbing species, A_t is the transition probability from the emitting to the absorbing state, and δ is a term used to correct for the relative half-widths of the emitting and absorbing spectra lines.

The ratio of incident (I_i) to transmitted (I_t) light is given by the expression[14-16]

$$\frac{I_i}{I_t}=\frac{\int_{-\infty}^{+\infty} I_0 f(\lambda)\, d\lambda}{\int_{-\infty}^{+\infty} I_0 f(\lambda) \exp[-k_0 l g(\lambda)]\, d\lambda} \tag{3}$$

where I_0 is the maximum intensity for the line at wavelength λ, $f(\lambda)$ is the emission profile, $g(\lambda)$ is the absorption profile, and l is the path length through which the transmitted light passes. The line profiles are assumed to be dominated by Doppler broadening; therefore, a Gaussian distribution is employed to describe the profiles.

For these experiments, $f(\lambda)=g(\lambda)$, as the absorbing and emitting species are at the same conditions. Therefore, a given $k_0 l$ corresponds to a given I_i/I_t for any spectral line so long as the integration limits in Eq. (3) are sufficiently large. Equation (3) was evaluated for several values of $k_0 l$, and expressions were obtained to relate $k_0 l$ to I_i/I_t over intervals of I_i/I_t.

Values for $k_0 l$ obtained from absorption data were related to the density of the absorbing states in the plasma jet. The length of optical path was taken to be equal to the plasma jet diameter at the point where absorption data were obtained. By assuming a parabolic distribution of absorbing species across of a jet of radius R, the absorbing state density at the center of the jet is given by

$$N_0=\frac{\sqrt[2]{2kT/m_a}\, 3\pi^{3/2} g_k k_0 l}{A_t \lambda^3 g_0 R} \tag{4}$$

with the Doppler half-width having been replaced by substituting the relation

$$\Delta\nu_D=\frac{1}{\lambda}\sqrt[2]{2kT \log_n(2)/m_a} \tag{5}$$

where T is the gas temperature and m_a is the mass of the absorbing species. The correction factor δ from Eq. (2) is taken to be unity since the line profiles overlap. Energy levels, transition probabilities, and statistical weights were compiled from the *CRC Handbook of Chemistry and Physics*.[17,18]

Incident and transmitted intensities, I_i and I_t, are obtained by comparing the integrated intensities measured over a given line profile for two cases, demonstrated in Fig. 2. In the first case, the reversing mirror is removed from the line of sight of the 45° mirror, and only the intensity $I_j(\lambda)$ is measured. In the second case, the reversing mirror is placed opposite the 45° mirror. The light emitted from the jet, $I_j(\lambda)$, is reflected off the mirror and becomes the incident intensity, $I_i(\lambda)$. Due to the increased path length for the light and reversing mirror efficiencies $\varepsilon(\lambda)$, I_i is always less than I_j.

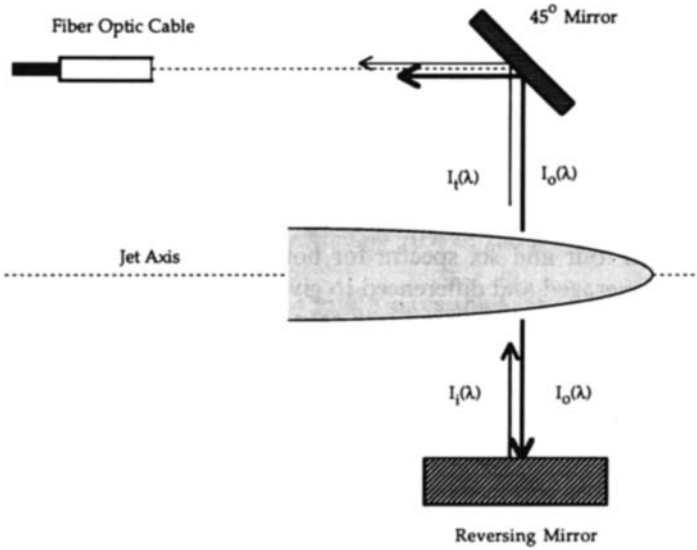

Fig. 2. Optical components employed in absorption experiments.

However, this can be accounted for to obtain I_i/I_t estimates for the various lines.

For a given line centered at λ, $I_i(\lambda)$ will be equal to $I_j(\lambda)$ times the wavelength-dependent mirror efficiency $\varepsilon(\lambda)$ and a geometric factor, α, which is constant for all wavelengths, so that

$$I_i(\lambda) = \alpha\,\varepsilon(\lambda) I_j(\lambda) \tag{6}$$

The net transmitted intensity is equal to the difference between the intensity measured along the reflected path $[I_r(\lambda)]$ and original jet intensities along the nonreflected path, that is,

$$I_t(\lambda) = I_r(\lambda) - I_j(\lambda) \tag{7}$$

Then

$$\frac{I_t(\lambda)}{I_i(\lambda)} = \frac{I_r(\lambda) - I_j(\lambda)}{\alpha\,\varepsilon(\lambda) I_j(\lambda)} \tag{8}$$

Defining the reflected fraction $f_r(\lambda)$ as

$$f_r(\lambda) = \frac{I_r(\lambda) - I_j(\lambda)}{\varepsilon(\lambda) I_j(\lambda)} \tag{9}$$

and assuming that $I_t(\lambda) = I_i(\lambda)$ for the most weakly absorbed (maximally reflected) line, for which the reflected fraction has its maximum value for all lines and is equal to α, then for all other lines,

$$\frac{I_i(\lambda)}{I_t(\lambda)} = \frac{\alpha}{f_r(\lambda)} \tag{10}$$

These I_i/I_t ratios are used to estimate $k_0 l$ values.

Between four and six spectra for both the reflected and nonreflected paths were averaged and differenced to give a mean transmitted fraction for each line. A standard deviation was calculated to estimate an uncertainty for the calculated absorbing state densities. The percent uncertainty, U, was estimated by adding a standard deviation to the line of interest and subtracting a standard deviation from the maximally reflected line, then calculating a second density, N_σ, from this I_t/I_i. The uncertainty is given by the expression

$$U(\%) = \frac{N_0 - N_\sigma}{N_0} \times 100\% \tag{11}$$

Other sources of error are the estimates for jet temperature and diameter, variation in detector performance, and the assumption of Doppler broadening only. Deviation of mirror reflectivity from manufacturer's specifications would introduce substantial error for those lines where the reflected fraction is within a few percent of the maximum reflected fraction. Most transition probabilities were reported to be accurate to within ±10–25%, although some have reported uncertainties between 25–50%.

3.3. Excited Argon Neutral Densities Estimated from Relative Line Intensities

Densities for excited argon neutrals above the 4*s* levels are estimated from line emission intensities for these levels relative to those for a selected 4*p* level. The absolute density of the 4*p* level is known from absorption measurements.

If a plasma is optically thin, then the photon flux $I(p, q)$ of a transition from state p to state q is given by the expression

$$I(p, q) = \frac{1}{4\pi} \int n(p) A(p, q)\, ds \tag{12}$$

where $I(p, q)$ is in units of photon flux per unit area per unit solid angle, $n(p)$ is the density of the emitting species p, $A(p, q)$ is the transition probability, and integration is over the observed depth of the plasma.[19]

An Abel inversion was not performed in this work. However, the cone observed by the fiber optic cable is narrow and the view normal to the jet axis is a cylinder of almost constant radius; this radius is approximately 1/2 the jet radius. If one assumes that the emission coefficient variation with radial position is described by a Gaussian profile, with the emission coefficient at the apparent jet perimeter equal to 1% of the coefficient at the jet axis, then the averaged emission coefficient over the circle defining the top of the view cylinder is approximately 70% of the emission coefficient at the axis.

Assuming that two species a and b have the same distribution across the observed path, then the ratio

$$\frac{I_a}{I_b} = \frac{n_a A_a}{n_b A_b} \tag{13}$$

is valid. However, each optical component between the plasma jet and the photodiode array has a reflectivity, transmittance, or quantum efficiency which depends on wavelength. Furthermore, absorption within the plasma jet must be corrected for. Therefore, two new parameters are introduced, the overall efficiency $\varepsilon(\lambda)$ and the transmitted fraction $\kappa(\lambda)$. The overall efficiency was defined as

$$\varepsilon(\lambda) = \Pi \varepsilon_i(\lambda) \tag{14}$$

with $\varepsilon_i(\lambda)$ the reflectivity for a mirror, transmittance of the optical fiber, or quantum efficiency of the photodiode array detector at the wavelength λ. From absorption data, a $k_0 l$ corresponding to a path traversing the entire jet was estimated. In this work, $\kappa(\lambda)$ is estimated as the transmitted fraction corresponding to $k_0 l/2$ for each line.

Correcting for differences in signal integration time t and rearranging Eq. (13) yields the expression

$$\frac{I_a}{I_b} = \frac{n_a A_a \varepsilon_a \kappa_a t_a}{n_b A_b \varepsilon_b \kappa_b t_b} \tag{15}$$

and the relative densities were obtained from the equation

$$\frac{n_a}{n_b} = \frac{I_a / A_a \varepsilon_a \kappa_a t_a}{I_b / A_b \varepsilon_b \kappa_b t_b} \tag{16}$$

Intensity and density for $4p$ levels from the absorption experiments and intensities measured for upper level transitions allow estimates for upper level densities from Eq. (16).

3.4. Electron Temperature and Density Measurements with Double Langmuir Probe

Electron densities and temperatures were estimated from the $V-I$ curves obtained from the double Langmuir probe, and the data were analyzed using the following relations:

$$kT_e = \frac{I_{is}e}{2(dI/dV)_{V=0}} \tag{17}$$

$$n_e = \frac{I_{is}}{eA}\sqrt[2]{m_i/kT_e} \tag{18}$$

where n_e and T_e are the electron density and temperature, respectively, I_{is} is the saturation current, e is the ion charge, A is the probe tip area, m_i is the ion mass, and k is Boltzmann's constant.

As Chen[20] points out, an advantage of the double probe is that the total collected current cannot exceed the ion saturation current; thus, localized distortion of plasma properties induced by the probe are minimal. The disadvantage is that double probes sample only the higher energy electrons, and not the bulk of the electron distribution. Consequently, the electron temperature is expected to be overestimated.

4. RESULTS

4.1. Jet Temperature and Velocity

Upon addition of methane, $T_{r,LL}$ are obtained from analysis of the $CH(A^2\Delta \rightarrow X^2\Pi)$ band structure at three axial positions downstream from the plasma jet entrance into the vacuum chamber. Estimated gas temperatures are 1100 K at 3.8 cm, 1160 K at 6.8 cm, and 1140 K at 8.9 cm. The $CH(A^2\Delta \rightarrow X^2\Pi)$ and $CH(B^2\Sigma \rightarrow X^2\Pi)$ bands were the dominant spectral features, with H_α and H_β lines quite weak by comparison. The bulk velocity for the plasma jet is calculated from the gas temperature, chamber pressure, argon flow rate, and estimated jet diameter. At the 3.8 cm axial position, the jet diameter is approximately 2.5 cm for 2000 sccm argon, 8.0 A, and chamber pressure of 560 mtorr (75 Pa). The estimated velocity is 350 m/s.

4.2. Electron Density and Temperature Measurements

Electron densities at the jet axis are shown as a function of axial position for various arc currents in Fig. 3. Initial n_e estimates at the jet inlet are in the range of $1.0\text{–}2.0 \times 10^{12}/\text{cm}^3$. For all currents the electron density dependence on axial position resembles a first-order decay. T_e estimates vary from

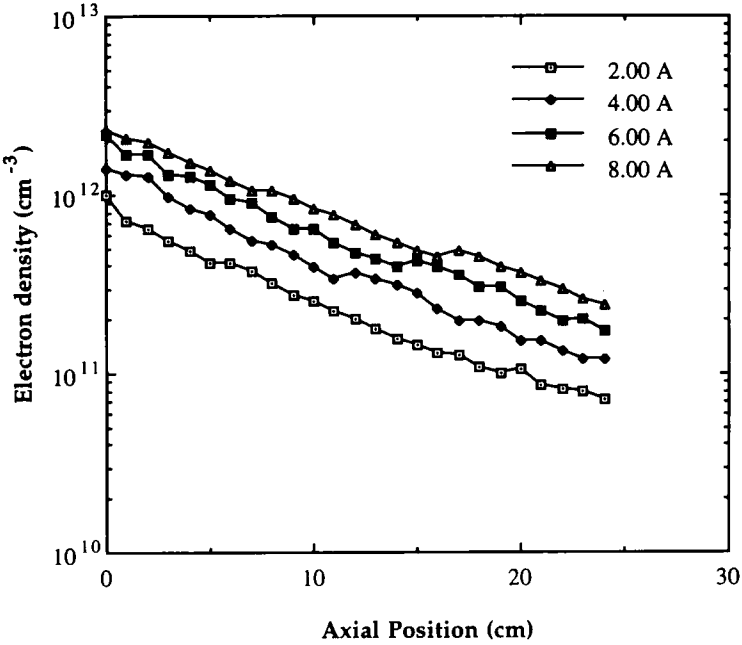

Fig. 3. Electron density (cm^{-3}) as a function of axial position and arc current. Other conditions are 2000 sccm argon and 560 mtorr (75 Pa).

1.0 to 2.0 eV, and are usually between 1.0–1.5 eV. However, as noted previously, T_e may be overestimated when employing Langmuir double probes.

4.3. Excited Neutral Density Estimates

Excited argon neutral densities estimated from absorption data for the 4*s* and 4*p* levels are given in Table I. 4*s* densities are in the range of about $1.0\text{–}5.0 \times 10^{11}/\text{cm}^3$, and 4*p* densities are of a similar magnitude. The ground-state density calculated from gas temperature and pressure measurements is $5.4 \times 10^{15}/\text{cm}^3$. The uncertainty due to variance in the data is between 10–15% for the 4*s* levels, and between 60–100% for the 4*p* levels. It is apparent that disagreement among the estimates for the 11.623 and 11.828 eV 4*s* levels are beyond that attributable to experimental error or uncertainty with respect to transition probabilities. Densities estimated using the 751.4652 and 750.3869 nm lines are a full order of magnitude below estimates for the same absorbing levels from other emitting levels. As these two transitions also have very high transition probabilities, the low estimates may be due

Table I. 4*s* and 4*p* Excited Argon Neutral Densities Determined at an Axial Position of 3.8 cm[a]

E(eV)	λ(nm)	n_E (cm^{-3})	U(%)	E(eV)	λ(nm)	n_E (cm^{-3})	U(%)
11.548	811.5311	3.35×10^{11}	15	12.906	687.1289	1.99×10^{11}	100
	801.4786	5.79×10^{11}	10		675.2834	4.22×10^{11}	90
	763.5106	3.12×10^{11}	10		641.6307	5.53×10^{11}	100
	696.5431	2.63×10^{11}	10	Root average		3.59×10^{11}	
Root average		3.55×10^{11}					
				13.076	703.0251	1.42×10^{11}	80
11.623	842.4648	4.01×10^{11}	10		603.2127	1.68×10^{11}	100
	810.3693	1.81×10^{11}	10		588.8584	3.71×10^{11}	100
	800.6157	6.40×10^{11}	10	Root average		2.07×10^{11}	
	751.4652	2.58×10^{10}	10				
Root average		1.86×10^{11}		13.095	604.3223	2.91×10^{11}	100
11.723	794.8176	3.76×10^{11}	10	13.283	610.5635	7.04×10^{11}	60
11.828	852.1442	7.37×10^{10}	10	13.302	720.6980	3.70×10^{11}	80
	840.8210	1.49×10^{11}	10				
	826.4522	7.13×10^{10}	15	13.328	629.6872	8.52×10^{11}	90
	750.3869	7.65×10^{9}	10				
Root average		4.95×10^{10}					

[a] Conditions are 5.0 A, 2000 sccm argon, and 75 Pa. Wavelength correspond to the line for which I_i/I_i data were obtained. No acceptable lines were available for the 13.153, 13.171, 13.273, and 13.480 eV levels.

to stimulated emission, in which two photons are emitted with the same direction and phase as the absorbed photon.

In order to estimate other excited argon neutral densities from relative intensities, $nA\varepsilon\kappa t/I$ values were calculated for four of the 4*p* levels from absorption and intensity data. These values are listed in Table II. Theoretically all of the values in Table II should be the same. However, errors are introduced due to the experimental uncertainty for estimated densities, transition probability uncertainties, and the approximate nature of the correction factor for absorption, κ. The $nA\varepsilon\kappa t/I$ value for the 12.906 eV level ($4p_1$) was chosen for density calculations, as there were three lines available

Table II. Estimated $nA\varepsilon\kappa t/I$ Values [see (16)] for Four of the 4*p* Excited Argon Neutral Levels[a]

Level	Energy (eV)	$nA\varepsilon\kappa t/I$ (cm^{-3})
$4p_1$	12.906	7.8×10^{14}
$4p_2$	13.076	4.3×10^{14}
$4p_3$	13.095	5.8×10^{14}
$4p_8$	13.302	1.8×10^{15}

[a] Jet conditions are 5.00 A, 2000 sccm argon, 560 mtorr (75 Pa), and axial position of 3.8 cm.

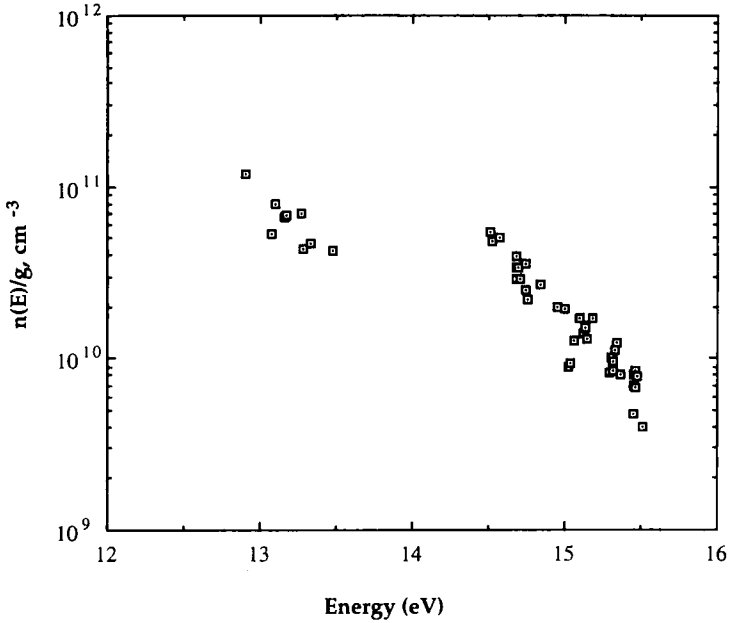

Fig. 4. A plot of $n(E)/g$ versus energy E for excited argon neutral densities estimated from relative intensity data. Conditions are 5.00 A, 2000 sccm argon, 560 mtorr (75 Pa), at an axial position of 3.8 cm.

for estimating the density from absorption and three lines available for estimating $nA\varepsilon\kappa t/I$ from emission intensities. The data were also most consistent for this level in comparison with the other 4*p* levels.

Integrated intensities were obtained for 46 energy levels at 4*p* or higher. (These energy levels are from data in the *CRC Handbook of Chemistry and Physics*.[17,18]) An extensive listing of the excited neutral argon energy levels is given by Minnhagen.[21]) Several of these levels had two or more lines which could be used to check for consistency, and the results were always within the uncertainty inherent from transition probabilities and experimental factors. A plot of n/g versus energy is given in Fig. 4. The sum of excited neutral densities from levels for which intensity data were available was $5.9 \times 10^{12}/\text{cm}^3$. When including approximate densities for 27 levels for which intensity data were not available (but could be approximated from the n/g values for neighboring levels of the same group), a total excited neutral density of $8.3 \times 10^{12}/\text{cm}^3$ was obtained. It must be noted that the 5*s* and 3*d* levels are, at present, completely omitted from the total estimates, as are several of the 6*p* and 7*p* levels and all of the 4*f*, 5*f* and 6*f* levels. This is due to the lack of any experimentally obtained data for these levels.

However, an estimate of the contributions of these levels to total excited argon neutral density is obtained by estimating n/g values from a Boltzmann plot through the experimentally obtained data points.

4.4. Methane Consumption in the Plasma Jet

When 20.0 sccm methane was added to the plasma jet (5.0 A, 2,000 sccm argon, and 560 mtorr), RGA data show that 25% of the methane disappears upon initiation of the plasma jet. Therefore, the flux of excited neutrals, ions and electrons in the plasma jet is sufficient to consume methane, directly or indirectly, at a rate of 5.0 sccm.

5. ANALYSIS

5.1. Factors Influencing the Population of Excited Argon Neutrals

The densities of excited neutrals relative to ground-state argon are much greater than would be predicted from the present estimate for a gas temperature of 1100 K. How the present distribution of excited argon neutrals is maintained at this relatively low temperature may be due to any of the following processes: (1) re-establishment of equilibrium among excited neutrals by collisions between electrons and excited neutrals, with the Boltzmann temperature equal to T_e, (2) repopulation of excited neutral levels by ion–electron recombination, (3) insufficient passage of time for relaxation via emission of radiation, and (4) trapping of radiation due to an optically thick environment.

5.1.1. Radiative versus Collisional Processes

The relative importance of electron collisions versus radiative transitions in maintaining the population of a given energy level depends on the rates at which collisional and radiative processes occur. Van der Mullen and Schram[9] derived the following rate constant expression for inelastic collisions between electrons and excited neutrals:

$$k(p) = 2.55 \times 10^{-8}(\text{cm}^3/\text{s})p^4 Z^{-2} T_e^{0.5} \tag{19}$$

where $k(p)$ is the rate constant, p is the principle quantum number, Z is the core charge, and T_e is the electron temperature in eV. Corrections to p which describe the nonhydrogenic behavior of argon are given in Ref. 9.

From an estimated T_e of 1.0 eV and n_e of 1.0×10^{12}/cm, and literature data for total transition probabilities $A(p)$, the ratio of radiative transitions to collisionally induced transitions is 440 for the $4s_2$ level and 36 for the $4p_1$

level. Clearly, electron collisions are of minor importance in establishing the population of these levels.

For higher energy neutrals, an approximate expression for $A(p)$ (also from Ref. 9) gives ratios of 2.9 and 0.3 for the $4d$ and $5d$ levels, respectively, assuming that the transitions are optically thick. Collisional dominance becomes increasingly pronounced at higher energy levels.

5.1.2. Three-Body Recombination

The three-body recombination rate constant for ionized argon varies from 1×10^{-26} cm^6/s at $T_e = 10{,}000$ K to 5×10^{-22} cm^6/s at $T_e = 1000$ K.[24] Using the largest rate coefficient and an estimated n_e of 1.0×10^{12}/cm^3, the initial recombination rate is 5.0×10^{14}/cm$^3 \cdot$ s, while the $4p_5$ level alone undergoes spontaneous transitions to the $4s$ levels at a rate of 1.0×10^{18}/cm$^3 \cdot$ s, based on the estimated $4p_5$ density of 3.4×10^{11}/cm^3. Three-body ion–electron recombination is clearly insufficient to offset spontaneous transitions from the $4p$ levels in an optically thin plasma.

5.1.3. Relaxation via Radiative Process

The degree to which radiation is trapped in the plasma jet is evaluated from estimated jet velocity, excited neutral densities, and relative intensities versus axial position. Over a distance of 15 cm, intensities for lines emitted from the $4p$ levels drop to 20% of the initial intensity, on average. Assuming that the average $4p$ densities along the 15 cm path are 60% of the initial densities, and from the total transition probability for the $4p$ levels, then 4.5×10^{19}/cm$^3 \cdot$ s transitions occur from the $4p$ levels to $4s$ levels throughout the jet volume. The total rate of $4p \rightarrow 4s$ transitions in an optically thin environment is estimated to be 3.3×10^{21}/s, compared with an estimated flux of excited neutrals (including levels estimated from the Boltzmann plot) of 2.4×10^{18}/s based on the present estimates for jet velocity (350 m/s) and jet diameter (2.5 cm). A jet velocity of 13,000 m/s would be required to balance the flux of excited neutrals versus radiative losses from the 15 cm length of the jet if it were optically thin. This is a full order of magnitude higher than any other estimates for jet velocity. Therefore, it is concluded that the plasma jet must be optically thick for the $4p$ levels.

As a further check on the trapping of $4p \rightarrow 4s$ transitions, a rough balance is performed for the $4s_2$ level at the 3.8 cm axial position. This particle balance is based on the assumptions that (1) convection is the dominant means of transport in the axial direction, (2) rate processes are adequately described by volume-averaged concentrations throughout the cylindrical control volume, and (3) all species except the ground-state neutrals have

Table III. Values for Diffusion Coefficients, Rate Constants, and Transition Probabilities Used in the Balance Calculations for $4s_2$ Argon Density and Electron Density[a]

D_{amb}		7100 cm^2/s
D_{exc}		1000 cm^2/s
k_r[22]	$Ar^+ + e^- + e^+ \rightarrow Ar^* + e^-$	5×10^{-23} cm^6/s
k_i[23]	$Ar^* + Ar^* \rightarrow Ar^+ + e^- + Ar$	5×10^{-10} cm^3/s
k_{2b}[24]	$Ar^* + Ar \rightarrow 2Ar$	4.0×10^{-15} cm^3/s
k_{3b}[24]	$Ar^* + 2Ar \rightarrow 3Ar$	1.9×10^{-32} cm^6/s
	$4p_1 \rightarrow 4s_2 + h\nu$	0.0543×10^8 s^{-1}
	$4p_3 \rightarrow 4s_2 + h\nu$	0.215×10^8 s^{-1}
	$4p_4 \rightarrow 4s_2 + h\nu$	0.25×10^8 s^{-1}
	$4p_5 \rightarrow 4s_2 + h\nu$	0.049×10^8 s^{-1}
	$4p_6 \rightarrow 4s_2 + h\nu$	0.402×10^8 s^{-1}
	$4p_8 \rightarrow 4s_2 + h\nu$	0.0847×10^8 s^{-1}
	$4p_9 \rightarrow 4s_2 + h\nu$	0.0183×10^8 s^{-1}

[a] References are cited next to the rates constants.

parabolic distributions in the radial direction. The particle balance equation is

$$v_z \frac{\Delta n}{\Delta z} + \frac{4Dn}{R^2} - \sum P_k = 0 \tag{20}$$

where v_z is the jet velocity (35,000 cm/s), $\Delta n/\Delta z$ is the particle density gradient in the axial direction, D is the diffusion coefficient, R is the jet radius (1.25 cm), and the P_k are the rate processes for consumption and production of $4s_2$ argon.

Coefficients for Eq. (20) are listed in Table III. The diffusion coefficient is estimated based on the experimental results of Kolts and Setser,[24] with the influence of optical thickness on "migration" of $4s_2$ argon by emission included.

Based on Eq. (20), experimental data, and the coefficients in Table III, the $4s_2$ density is predicted to increase at an initial rate of $3.1 \times 10^{14}/cm^3$ with each centimeter in axial position, versus an observed average decrease between 3.8 and 8.8 cm of $7.0 \times 10^9/cm^3$ per cm. The major paths for $4s_2$ loss are by diffusion ($8.0 \times 10^9/cm^3$ per cm) and ionizing collisions with other excited argon neutrals ($6.3 \times 10^9/cm^3$ per cm). All other loss routes are negligible. To obtain the observed decay rate, on average only one in every 25,000 $4p \rightarrow 4s_2$ transitions results in the net production of $4s_2$ argon, while the remainder are absorbed by other $4s_2$ argon and repopulate the respective $4p$ level. This requires a $k_0 l$ of about 10, while the largest $k_0 l$ from absorption measurements was about 3. However, these $k_0 l$ were across the

shortest possible path. For photons emitted at an angle to the radial coordinate, the optical thickness of the jet will increase markedly.

5.2. Temperature Estimates from Boltzmann and Saha Equations

A linear least squares fit of $\log_n(n/g)$ *vs.* E (a Boltzmann plot) for the $4p$ levels and higher gives an estimated Boltzmann temperature of 12,700 K for the conditions cited in Table II. Extrapolation of this fit to $E=0$ gives a ground-state neutral density of $1.4\times10^{16}/\text{cm}^3$, while the ground-state density estimated from chamber pressure and gas temperature is $5.4\times10^{15}/\text{cm}^3$. Temperatures estimated from the Boltzmann equation for various excited levels versus the ground state lie in the 12,000–13,000 K range, with a few yielding higher temperature estimates. As an indication of the accuracy of this estimate, a temperature of 10,000 K in the Boltzmann equation would give n/g values of $1.5\times10^{8}/\text{cm}^3$ for levels near 15.0 eV, almost two orders of magnitude less than the $1\times10^{10}/\text{cm}^3$ obtained in the present work. Estimated contributions from 5s, 3d, 4–6*f*, and omitted $6p$ and $7p$ levels bring the total estimated excited argon density to $1.4\times10^{13}/\text{cm}^3$ for the conditions cited in Table I. Contributions from excited neutrals near the ionization energy are not included, as this would require extrapolation of the Boltzmann plot into energy levels for which scant experimental data are available. A Boltzmann plot through the $4d$, $5p$, and $5d$ levels in Fig. 4 yields a temperature of 5100 K. Calculations from Eq. (19) predict that electron collisions will begin to dominate radiative transitions in establishing the distribution function among these levels. Therefore, this Boltzmann temperature from the distribution among upper levels may be representative of the electron temperature.

The Saha equation,

$$\frac{n_A^S(p)}{g(p)}=\frac{n_e n_+}{2g(+)}\frac{h^3}{(2\pi m_e kT)^{3/2}}\exp(E_p/kT) \tag{21}$$

allows a temperature to be estimated from electron density data and the density for any state with an ionization potential E_p. This equation can also be used to calculate a departure coefficient, which is defined here as the ratio of the actual density $n(p)$ to the density predicted on the basis of the Saha equation, $n_A^S(p)$ for a given temperature and electron density. For either temperature estimate from Boltzmann plots (12,500 or 5100 K), the departure coefficients for energy levels between 11.5–15.5 eV range from 10^5 to 10^8, with departure coefficients for the 15.5 eV levels between 10^6–10^7. Clearly, Saha equilibrium is not established for these excited levels, even for levels within 0.26 eV of the ionization potential.

5.3. Evaluation of Ion Production and Loss Processes in the Plasma Jet

In order to evaluate the self-consistency of measurements for electron density, excited neutral densities, and jet velocity, Eq. (20) is used to perform a balance on electron density over the plasma jet at an axial position of 3.8 cm. The ambipolar diffusion coefficient and rate constants are given in Table III. The rate constant for ionizing collisions among excited neutrals is for collisions among 4*s* levels, and is assumed valid for the higher levels. The volume-averaged electron and excited neutral densities are $1 \times 10^{12}/\text{cm}^3$ and $7 \times 10^{12}/\text{cm}^3$, respectively. v_z and R are the same as for the $4s_2$ calculations. The volume-averaged production rates for n_e are $-5.2 \times 10^{11}/\text{cm}^3$ per centimeter of travel along the jet axis from ambipolar diffusion, $+7.0 \times 10^{11}/\text{cm}^3$ from ionizing excited neutral collisions, and $-1.4 \times 10^{9}/\text{cm}^3$ from three-body recombination, giving a net production of electrons of $+1.8 \times 10^{11}/\text{cm}^3$ per centimeter of travel along the jet axis, versus an experimental measurement of $-2.6 \times 10^{11}/\text{cm}^3$ from the Langmuir probes. This calculation shows that the loss of charged particles by ambipolar diffusion is offset by ionizing collision, while three-body recombination is a negligible route for charged particle losses. Although measurements show loss of charged particles rather than gain, the magnitude of the disagreement between measured and predicted electron losses is well within the cumulative uncertainty for the parameters used in the calculation.

5.4. Comparison of Methane Consumption with Excited/Ionized Argon Flux

The total flux of excited and ionized argon is $8.8 \times 10^{17}/\text{s}$ at an axial position of 3.8 cm for conditions of 5.0 A, 2000 sccm Ar, and chamber pressure 560 mtorr (75 Pa). Under these same conditions, with 20.0 sccm methane added to the plasma jet, the rate of methane consumption estimated from residual gas analysis is $2.2 \times 10^{18}/\text{s}$. This is 2.5 times the total flux of excited and ionized argon.

Methane reacts rapidly with excited and ionized argon. The rate constant for charge transfer between argon ions and methane is 1.03×10^{-9} cm^3/s.[25] Collision cross-sections estimated for the quenching of 4*s* argon by methane[26-28] give rate constants of roughly 1.0×10^{-9} cm^3/s at a jet temperature of 1100 K. All excited argon neutrals at the 4*p* level or higher can react with methane by excitation transfer or Penning ionization.

The dissociation paths for methane with energy requirements closest to the energy available from excitation transfer or dissociative recombination give H, H_2, and excited CH as the major products. This is consistent with experimental observations, as emissions from excited CH are by far the dominant spectral features.

Each excited or ionized argon will react rapidly with methane, producing methane ion or methyne radical. The rate constant for proton transfer from methane to ionized methane is 1.5×10^{-9} cm^3/s.[29] The rate constants for dissociative recombination of CH_4^+ and CH_5^+ are both 8.0×10^{-8} cm^3/s.[30] The rate constant for attachment of methyne radical to methane is 1.0×10^{-10} cm^3/s.[31,32] The relatively slow methyne–methane reaction leads to the consumption of 99.9% of the methyne over the length of the reactor. The ionized CH_x species will undergo dissociative recombination at an even faster rate. Therefore, methyne and ionized CH_x species are completely removed from the gas phase before the gas phase exits the vacuum chamber.

From these reactions, the number of methane molecules consumed due to each charge or excitation transfer from argon to methane will be between 2 and 3, depending on the degree to which excitation transfer caused Penning ionization and the competition between dissociative recombination and proton transfer for consumption of CH_4^+. Other reactions, such as hydrogen abstraction by atomic hydrogen, are negligible at the estimated gas temperature.

The observed ratio of methane consumption versus excited/ionized argon flux of 2.5 is in good agreement with the predicted ratio of between 2–3. This leads us to conclude that the estimated fluxes of excited and ionized argon are accurate, and that estimated particle densities, gas temperature, and jet velocity are self-consistent.

6. DISCUSSION

6.1. Comparison of Present Measurements with Literature Values

The estimated gas temperatures of 1100–1160 K are much lower than those estimated by Koulidiati *et al.*[33] and Beulens,[2] who also analyzed the CH band and obtained estimated T_{rot} between 2600–3100 K. Kroesen's[1] temperature estimates from Doppler widths were also considerably higher than the present estimates, ranging from 2000–4500 K across the jet radius.

The present estimates for gas temperatures may be lower due to different experimental conditions and different methods for estimating the temperatures from diagnostic data. In the cited works, an arc current of 50 A was used versus 8.0 A in the present work. The present assumption that $R(1, 1)$ and $Q(0, 0)$ contributions are negligible for the rotational levels analyzed is expected to give low estimates for gas temperature. On the other hand, the approach by Koulidiati *et al.*[33] and Beulens[2] assumes that a single rotational temperature adequately describes the entire $CH(A^2\Delta \rightarrow X^2\Pi)$ band structure. Suzuki and Kuchitsu[11] demonstrated that the band structure of

$CH(A^2\Delta \rightarrow X^2\Pi)$ from methane dissociated in an argon afterglow is more accurately described by a two-temperature model. Therefore, the temperatures calculated by Koulidiati *et al.*[33] and Beulens[2] may be overestimated.

The jet velocity estimate of 350 m/s is somewhat below the estimates of Kroesen[1] (500–2000 m/s). This may be attributed to the higher current and flow rate employed (50 A, 6000 sccm) by Kroesen.

Present estimates of electron temperature from the Langmuir double probe range from 1.0 to 2.0 eV. De Graaf *et al.*[34] found T_e between 0.3–0.6 eV from double probe measurements in the expansion of a cascade arc argon plasma jet with hydrogen at chamber pressures between 0.4–1.0 Torr (52–133 Pa), and Beulens' model of the expansion[2] predicts electron temperatures of about 0.5 eV in the expansion. As noted previously, the slope of a Boltzmann plot through the upper levels yields a temperature near 0.5 eV, with excited neutral collisions with electrons predicted to outweigh radiative transitions as the process through which the distribution of these levels is populated.

Electron densities in the first 10 cm of the expansion are between $2 \times 10^{12}/cm^3$ and $3 \times 10^{11}/cm^3$, roughly an order of magnitude below those n_e estimated by Kroesen[1] from Stark broadening measurements for the plasma jet at an axial position of 3.0 cm and jet conditions of 50 A, 6000 sccm argon, and 750 mtorr (100 Pa). Since Kroesen was working with currents and argon flow rates greater than those used in the present work, the present n_e measurements are considered reasonable in comparison.

No measurements for excited neutral densities or the relative distribution of excited states in a cascade arc plasma jet are available in the literature.

6.2. Comparison of the Plasma Jet ASDF with Model Predictions

On the basis of van der Mullen's classification of departures from thermodynamic equilibrium (TE), [8] we consider local TE(LTE) and partial LTE (pLTE) as models to describe the plasma jet ASDF. When TE exists, all of the balances (Maxwell, Boltzmann, Saha, and Planck) are in equilibrium. For LTE, the Planck balance no longer applies, but the other balances do apply and all material particles (neutrals, ions, and electrons) have the same translational temperature within a limited spatial domain. For pLTE, equilibrium between recombination and ionization exists for a limited portion of the ASDF, with the Boltzmann and Saha balances coming into equilibrium only for excited neutrals in some excited states approaching the ionization potential. The temperature obtained from a Boltzmann plot through these levels should correspond to the electron temperature, while the distribution of lower energy levels will not. Furthermore, this temperature should hold in the Saha balance, too, with a departure coefficient near

1 for all excited levels in Saha equilibrium with the successive ionization stage.

From the present results, it is clear that none of these models offer a satisfactory basis for description of the cascade arc plasma jet. LTE does not exist, as the gas, Boltzmann, and electron temperatures all differ. Furthermore, pLTE is not satisfied for any portion of the ASDF established by optical emission data, as the departure coefficient (calculated from measurements for excited neutral densities, n_e and T_e) is several orders of magnitude greater than 1 for all excited neutrals. It is concluded that this particular plasma jet (and perhaps most low-pressure plasma jets) are not adequately described by these conventional plasma models.

The departure from pLTE observed in the present system is due to an optically thick jet for the $4s$ and $4p$ levels (at least), and the rapid loss of charged particles from the plasma jet by ambipolar diffusion. Absorption processes pin the lower-level densities at the resonance radiation temperature, while collisions with electrons repopulate the upper levels from the optically thick lower levels. Collisions between electrons and upper-level excited neutrals may occur with sufficient frequency relative to radiative processes to impose the electron temperature upon the distribution of upper levels, but the frequency of collisions is clearly insufficient to establish equilibrium between the upper levels up to 15.5 eV and the first ionization stage. Ionizing collisions among excited neutrals almost balance diffusional losses of electrons.

These results support the assertion by Chang and Pfender[10] that low-pressure argon plasma jets are non-LTE. Furthermore, the results show that successful modeling of these jets will require measures which account for the influence of optically thick transitions through the $4p$ levels, perhaps to within 1 eV of the ionization potential.

7. CONCLUSIONS

Based on particle density estimates, it is concluded that excited argon neutrals outnumber argon ions by a large ratio, and therefore will dominate monomer dissociation processes in the plasma jet. Excited neutral densities are sufficiently high that the jet is optically thick and the excited neutral densities decay quite slowly.

The plasma jet is nonequilibrium. The estimated gas temperature is 1100 K. The temperature estimated from excited neutral density ratios (assuming a Boltzmann distribution) is between 12,000–13,000 K. Saha equation calculations give departure coefficients between 10^5–10^8 for excited neutrals. The dominant spectral features upon addition of methane to the plasma jet are the CH($A^2\Delta \rightarrow X^2\Pi$) and CH($B^2\Sigma \rightarrow X^2\Pi$) transitions, which

is consistent with the energy available from excitation transfer with argon and the dissociative recombination of ionized methane.

The present work confirms the predictions of Chang and Pfender[10] regarding the unsuitability of the LTE assumption for low-pressure argon plasma jets. Furthermore, pLTE does not provide a satisfactory description of the ASDF, either. Particle densities must be measured explicitly, as they cannot be satisfactorily inferred from other temperatures or particle densities.

ACKNOWLEDGMENTS

The authors are indebted to J. Javedani, J. Chiang, and M. Prelas for performing the Langmuir probe measurements. We are also indebted to D. C. Schram, J. J. Beulens, and their colleagues at EUT for generously sharing their expertise in this area. This work was supported by PlasmaCarb, Inc.

REFERENCES

1. G. M. W. Kroesen, Ph.D. Thesis, Eindhoven University of Technology, Eindhoven, The Netherlands (1988).
2. J. J. Beulens, Ph.D. Thesis, Eindhoven University of Technology, Eindhoven, The Netherlands (1992).
3. J. J. Beulens, G. M. W. Kroesen, D. C. Schram, C. J. Timmermans, P. C. N. Crouzen, H. Vasmel, H. J. A. Schuurmans, C. B. Beijer, and J. Werner, *J. Appl. Polym. Sci.: Appl. Polym. Symp.* **46**, 527 (1990).
4. G. M. W. Kroesen, D. C. Schram, and M. J. F. van de Sande, *Plasma Chem. Plasma Process.* **10**, 49 (1990).
5. J. J. Beulens, A. J. M. Buuron, L. A. Bisschops, T. H. J. Bisschops, A. B. M. Husken, G. M. W. Kroesen, G. J. Meeusen, C. J. Timmermans, A. T. M. Wilbers, and D. C. Schram, *Colloq. Phys.* **51**, C5-361 (1990).
6. A. J. M. Buuron, J. J. Beulens, R. J. F. van de Sande, D. C. Schram, and J. G. van der Laan, *Fusion Tech.* **19**, 2049 (1991).
7. J. A. M. van der Mullen, *Spectrochim. Acta* **44B**, 1067 (1989).
8. J. A. M. van der Mullen, *Spectrochim. Acta* **45B**, 1 (1990).
9. J. A. M. van der Mullen and D. C. Schram, *Spectrochim. Acta* **45B**, 233 (1990).
10. C. H. Chang and E. Pfender, *Plasma Chem. Plasma Process.* **10**, 473 (1990).
11. K. Suzuki and K. Kuchitsu, *Bull. Chem. Soc. Jpn.* **50**, 1905 (1977).
12. I. Botterud, A. Lofthus, and L. Veseth, *Phys. Scr.* **8**, 218 (1973).
13. A. C. G. Mitchell and M. W. Zemansky, *Resonance Radiation and Excited Atoms*, University Press, Cambridge (1961).
14. N. P. Ferreira and H. G. C. Human, *Spectrochim. Acta* **36B**, 215 (1981).
15. C. S. Rann, *Spectrochim. Acta* **23B**, 443 (1968).
16. C. S. Rann, *Spectrochim. Acta* **23B**, 827 (1968).
17. W. L. Wiese and G. A. Martin, in *CRC Handbook of Chemistry and Physics*, 62nd ed., R. C. Weast, ed., CRC Press, Boca Raton (1981).
18. J. R. Fuhr and W. L. Wiese, in *CRC Handbook of Chemistry and Physics*, 71st ed., D. R. Lide, ed., CRC Press, Boca Raton (1990).

19. R. W. P. McWhirter, in *Plasma Diagnostic Techniques*, R. H. Huddleston and S. L. Leonard, eds., Academic Press, New York (1965).
20. F. F. Chen, in *Plasma Diagnostic Techniques*, R. H. Huddleston and S. L. Leonard, eds., Academic Press, New York (1965).
21. L. Minnhagen, *J. Opt. Soc. Am.* **63**, 1185 (1973).
22. J. V. Dugan, Jr., *J. Appl. Phys.* **37**, 5011 (1966).
23. M. McCusker, in *Excimer Lasers*, C. K. Rhodes, ed., Springer-Verlag, New York (1984).
24. J. H. Kolts and D. W. Setser, *J. Chem. Phys.* **68**, 4848 (1978).
25. J. B. Laudenslager, W. T. Huntress, Jr., and M. T. Bowers, *J. Chem. Phys.* **61**, 4600 (1974).
26. J. E. Velazco, J. H. Kolts, and D. W. Setser, *J. Chem. Phys.* **69**, 4357 (1978).
27. J. LeCalve, R. A. Gutcheck, and O. Dutuit, *Chem. Phys. Lett.* **47**, 470 (1977).
28. H. J. DeJong, *Chem. Phys. Lett.* **25**, 129 (1974).
29. D. Smith and N. G. Adams, *Int. J. Mass Spectrom. Ion Phys.* **23**, 123 (1977).
30. P. M. Mul, J. B. A. Mitchell, V. S. D'Angelo, P. Defrance, J. W. McGowan, and H. R. Froelich, *J. Phys. B.* **14**, 1353 (1981).
31. S. J. Harris, *J. Appl. Phys.* **65**, 3044 (1989).
32. M. R. Berman and M. C. Lin, *Chem. Phys.* **82**, 435 (1983).
33. J. Koulidiati, A. Czernichowski, J. J. Beulens, and D. C. Schram, *Colloq. Phys.* **51**, C5-297 (1990).
34. M. J. de Graaf, R. P. Dahiya, J. L. Jauberteau, F. J. de Hoog, M. J. F. van de Sande, and D. C. Schram, *Colloq. Phys.* **51**, C5-387 (1990).